Advanced Energy Conversion Materials
http://ojs.wiserpub.com/index.php/AECM/

UNIVERSAL WISER PUBLISHER

Research Article

# Optimization of the MA/FA Ratio in the Structure of Absorber Layers Based on $MA_{(1-x)}FA_xPbI_3$ Perovskites for Stable and Efficient Solar Cells

**Idrissa Diomandé[1,2*], Amal Bouich[1], Mina Nezamisavojbolaghi[2,3], Mouhaydine Tlemçani[2,3], Bernabe Mari Soucasse[1], Aka Boko[4]**

[1]Institute of Design and Manufacturing, Polytechnic University of Valencia, Valencia, Spain
[2]Instrumentation and Control Laboratory, Institute of Earth Science, Évora, Portugal
[3]Department of Mechatronics Engineering, University of Évora, Évora, Portugal
[4]Laboratory of Fundamental and Applied Sciences, Nangui Abrogoua University, Abidjan, Ivory Coast
E-mail: idiomande13@yahoo.fr

**Received:** 20 July 2023; **Revised:** 28 September 2023; **Accepted:** 8 October 2023

**Abstract:** Herein, we investigate the mixture of methylammonium lead iodide ($MAPbI_3$) and formamidinium lead iodide ($FAPbI_3$). The perovskite films were coated onto fluorine-doped tin oxide (FTO) glass substrates using a spin-coating method, with the spin-coater set at 4,000 rpm for 20 s. We studied the influence of incorporation in $MA_{(1-x)}FA_{(x)}PbI_3$ films. The crystal structure of the perovskite films was characterized using X-ray diffraction (XRD). Optical properties were assessed using UV-Vis spectroscopy with a spectrophotometer, and photoluminescence (PL) was characterized using a He-Cd Si-CCD laser source and a Hamamatsu detector. Images depicting the characteristic morphology of the films were captured with a scanning electron microscope (SEM). Our measurements reveal that the crystallinity of the $MAPbI_3$ thin film improved with the incorporation of $FAPbI_3$. In the case of 70% $FAPbI_3$, the morphology of the $MA_{30}FA_{70}PbI_3$ mixture also improved, exhibiting a rough surface with pores. The optical properties were enhanced, and the mixed thin film demonstrated better stability compared to pure $MAPbI_3$ and $FAPbI_3$ thin films. These film characteristics indicate that the mixtures are particularly suitable for use in photovoltaic applications.

***Keywords***: perovskites, FA, MA, stability, solar cell

## 1. Introduction

Perovskite-based solar cells have demonstrated significant advancements in photovoltaic conversion. They possess a structure of the form $ABX_3$, where A represents a monovalent cation ($MA^+$, $Cs^+$, $FA^+$ …) B denotes a divalent cation ($Pb^{2+}$, $Sn^{2+}$, $Ge^{2+}$, or $Cu^{2+}$) and X stands for a halide anion ($I^-$, $Cl^-$, $Br^-$ or $O^-$ …) [1]. Their conversion efficiency has markedly improved over the past few years, rising from 3.8% to 25.2%. Furthermore, they exhibit absorption capabilities across the visible spectrum [2-5] and can be easily synthesized from abundant and inexpensive materials [6]. Perovskite thin films can be fabricated using various techniques, including one-step solution deposition, two-step solution-assisted deposition [7], vapor phase deposition [8], Quantum Dot, and blade [9]. In this study, we employed a one-step deposition method using centrifugation. The low-temperature synthesis technique of perovskites enables


DOI: https://doi.org/10.37256/aecm.4220233405

their utilization in various applications, such as electronic band gap tuning, medical radiography, light-emitting diodes (LEDs) [10], the degradation of organic dyes, and water separation reactions [11]. With a tunable band gap, low processing costs, excellent optoelectronic properties, long useful carrier diffusion length in solar cells, and high carrier mobility, perovskites exhibit significant potential as an innovative next-generation solar technology [12]. Despite these attractive potentials, the main disadvantage concerns the durability of the perovskite material, attributed to its instability in response to various external factors, including humidity, oxygen, high temperatures, and ultraviolet light [13]. Additionally, the presence of lead in the perovskite structure poses environmental concerns [14]. Therefore, perovskites offer ample opportunities for optimization. Strategies such as whole-cell encapsulation and surface engineering are employed to enhance film stability. These extrinsic strategies prevent the films' surfaces from interacting with the atmosphere but do not provide intrinsic solutions for delaying degradation throughout the thin film [15]. Effective stabilization of the perovskite layers' interior is crucial. Within the extensive perovskite family, the organic halides 1,4 Methylammonium lead tri iodide $(CH_3NH_3)PbI_3$ or $MAPbI_3$ and Formamidinium lead iodide $HC(NH_2)_2PbI_3$ or $FAPbI_3$ show particular promise. Studies on $MAPbI_3$ materials focus on mixing $MAPbI_3$ with $FAPbI_3$ and other potentially more stable absorbers. Research has concentrated on combining the organic cations MA and FA to create compounds of the $MA_{(1-x)}FA_xPbI_3$ type [16-20]. Indeed, $MAPbI_3$ is the most widely used photon absorber; it remains stable under ambient conditions but has a high band gap (2.8 eV) [21]. Furthermore, $FAPbI_3$ possesses a smaller band gap of around 1.47 eV, exhibits thermal stability, and has greater resistance to ultraviolet light compared to $MAPbI_3$ [22]. $MA_{(1-x)}FA_x$ organic monocation mixtures enable FA to crystallize in the desired dark phase and extend absorption to longer wavelengths [23]. The best yields obtained with $MA_xFA_{(1-x)}PbI_3$ type perovskites are approximately 21.38% [24]. The objective of this work was to provide insights into the effects of optimizing the MA/FA ratio in $MA_{(1-x)}FA_xPbI_3$ perovskites on stability, conversion efficiency, and material properties. The optical properties of the perovskite films obtained revealed that the inclusion of FA in the $MAPbI_3$ structure reduces the width of the bandgap and decreases the degradation rate of the mixed perovskites. Additionally, an enhancement in sample absorption is observed. We recommend considering the perovskite mixture $MA_{0.3}FA_{0.7}PbI_3$ as a more stable material than pure $MAPbI_3$ and $FAPbI_3$, which could be utilized as an absorber layer in solar cells. The purpose of this work is to determine the optimal MA and FA ratio where the perovskite material exhibits higher absorption and good stability under extreme environmental conditions.

## 2. Materials and experimental procedure

### 2.1 *Materials*

All precursor chemicals were purchased from Sigma Aldrich, St. Louis, MO, USA, and were used for the synthesis of $MA_{(1-x)}FA_xPbI_3$ perovskites without prior refining. To deposit the layers, the perovskite solutions used contained different masses of three precursors: Methylammonium iodide (MAI) at a concentration of 99.99%, Formamidinium iodide (FAI) at a concentration of 99.99%, and lead (II) iodide ($PbI_2$) at a concentration of 99.99%. The perovskite solutions were prepared in small, very dark brown bottles (to prevent the solutions from reacting with light) by dissolving the $PbI_2$, FAI, and MAI precursors in a mixture of anhydrous N, N-dimethylformamide $DMF_{0.9}$ and Dimethylformamide $DMSO_{0.1}$. and dimethylsulfoxide Chlorobenzene (or toluene) was used as an anti-solvent.

### 2.2 *Films preparation*

The perovskite films were produced on clean fluorine-doped tin oxide (FTO) glass substrates. The substrates were washed with Hellmax soap in distilled water and rinsed with ethanol and acetone; all of these washing operations were performed using ultrasound. Organic matter was removed with UV-Ozone. To prepare the $PbI_2$ solutions, 1 ml of the solvent mixture ($DMF_{0.9}$ and $DMSO_{0.1}$) was used to dissolve 0.461 g of $PbI_2$ in a small dark brown bottle. The solutions obtained were kept on a hot plate at 60 °C for two hours. To create the perovskite solutions, each sample shown in Figure 1 contains a mixture of $MAI_{(1-x)}$ and Les $FAI_{(x)}$, to which 1 ml of the $PbI_2$ solution was added. The different $MA_{(1-x)}FA_xPbI_3$ solutions were then deposited onto the rotating substrate using the one-step spin-coating method. The number of precursors used was calculated using Eq. 1.

$$(1\text{-}x)\ MAI + xFAI + PbI_2 - MA(1\text{-}x)\ FAxPbI_3 \quad (1)$$

With x = {0; 0.25, 0.5, 0.75, 1} the FA portion. Figure 1.

The solutions were heated at 60 °C for two hours. Then, 100 µL of perovskite solution was used to coat the FTO glass substrate by spin-coating at 4,000 rpm for 20 s. The thickness of the thin film deposited is estimated to be between [insert estimated thickness]. During this operation, a few drops of chlorobenzene (or toluene) were deposited onto the wet perovskite films. Finally, the perovskite deposits obtained were thermally annealed at 110 °C for 20 minutes on a hot plate.

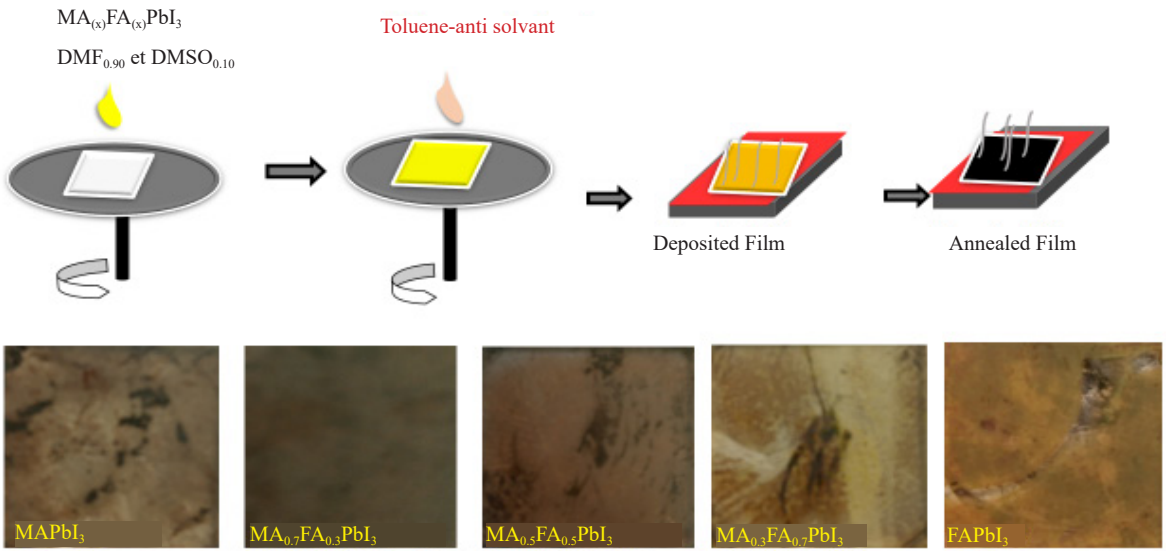


**Figure 1.** Synthesis procedures and sample photographs of $MA_{(1-x)}FA_xPbI_3$ perovskite films

## 2.3 *Lattice parameters*

The parameters were calculated using the following Bragg's equations:

$$\frac{1}{d^2} = \frac{h^2 + k^2}{a^2} + \frac{l^2}{c^2} \quad \text{and} \quad n\lambda = d\,2\sin(\theta) \quad (2)$$

$h$, $k$, $l$: Miller indices and $a$ and $c$ are lattice constants,
$d$: Inter-planar-spacing,
$a$, $c$: Lattice constants,
$\lambda$: Wavelength of the CuK α radiation (0.154 nm),
$2\theta$: Difraction angle of the corresponding plane.

### 2.3.1 *Grain size and effective lattice strain*

The calculation of the effective grating deformation provides an overview of defects and distortions within the grains in the film. We use the following equation for this calculation:

$$\cos\theta\beta_r = 4\varepsilon\sin\theta + \frac{k\lambda}{D} \quad (3)$$

$k$: Constant whose value is 0.94,
$\lambda$: 0.15406 nm wavelength of the X ray source,
$D$: Crystallite size or half-width (FWHM),
$\varepsilon$: Deformation,
$\theta$: Position of the peak in radians where is the Bragg angle.

### 2.3.2 *Dislocation density*

The dislocation density of the crystal was evaluated using the following formula:

$$\gamma = \frac{1}{D^2} \quad (4)$$

### 2.3.3 *Absorption coefficient*

Perovskites are direct band gap semiconductors. the energy band gap is calculated from an estimate of the trace$(\alpha hv)^2$ with respect to $hv$.

$$(\alpha hv)^2 = B(hv - Eg) \quad (5)$$

$$\alpha = \frac{1}{t}\ln\left(\frac{1}{T}\right) \quad (6)$$

$\alpha$: Absorption coefficient,
$h$: Planck constant,
$Eg$: Forbidden band energy,
$t$: Thickness of the layers,
$B$: Constant.

## 3. Results and discussions

To confirm the production of perovskite materials, XRD measurements (λ = 1.54 Å) were performed on $MA_{(1-x)}FA_xPbI_3$ mixes. The methylammonium cation is suitable for lead halide perovskite because its ionic radius is 1.8 Å. The formamidinium ion has a slightly larger ionic radius than the methylammonium group (RA = 0.18 nm for $MA^+$ and 0.19-0.22 nm for $FA^+$, respectively).

As depicted in Figure 2 the prominent characteristic peaks of $MAPbI_3$ at 2θ angles of 14.16° (110), 28.57° (220), and 31.54° (310) serve to confirm the complete formation of $MAPbI_3$ within the perovskite film [25]. Figure 2 displays XRD spectra for $MAPbI_3$, $FAPbI_3$ films, and $MA_{(1-x)}FA_xPbI_3$ mixtures. In both $MAPbI_3$ and $FAPbI_3$ spectra, the 2θ value of 12.80 corresponds to residual $MAPbI_2$ that remains unreacted. Notably, the peaks attributed to FTO are observed at approximately 26.54°, 37.83°, and 51.55° [26].

Characteristic peaks within the $MAPbI_3$ spectrum are identified at 2θ values of 14.24° and 28.57°, corresponding to the planar orientations of (110) and (220), representing parallel planes within the perovskite structure. These peaks indicate a preferential growth of this layer in the tetragonal direction. Similarly, average peaks are detected at 2θ positions of 31.54°, 40.74°, and 43.74°, corresponding to planar orientations (314), (214) in the orthorhombic phase, and (330) in the tetragonal phase. The 2θ values for the peaks identified in the mixture diagrams exhibit gradual variations.

Indeed, the incorporation of MA and FA cations into the same lattice results in a gradual shift of the diffraction angle [27]. Consequently, the peaks at 14.16, 28.59, 31.54, 40.74, and 43.74 gradually shift towards lower diffraction angles as the FA content increases. This shift is attributed to the larger size of the MA/FA mono-cation mixture and the expansion of the network caused by it.

The XRD spectrum of $FAPbI_3$ reveals the presence of the desired alpha phase (α) as well as the black gamma phase (δ), which is orthorhombic. Its spectrum exhibits peaks similar to those in the spectra of the mixtures. The intensities are located at positions 10.14 and 14.06, corresponding to the planes (001) δ - $FAPbI_3$ (unstable) and (001) α - $FAPbI_3$ (pure, stable) [28]. Additionally, there are mean peaks at 28.17, 31.95, 40.28, and 42.78, corresponding to the planar orientations (002), (012), (022), and (033).

The diffraction spectra indicate that the blending of $FAPbI_3$ and $MAPbI_3$ affects the quality of the perovskites [29]. In the diffraction spectrum of the film mixture, there is a very small amount of $PbI_2$ residue. Notably, the $MA_{0.7}FA_{0.3}PbI_3$ mixture demonstrates nearly complete conversion, with clearly discernible peaks matching the reference peaks and an almost negligible presence of residues. In contrast, the $MA_{0.3}FA_{0.7}PbI_3$ mixture exhibits fewer peaks than the other spectra, with a prominent peak at 12.6, representing $PbI_2$ residues.

**Table 1.** values of the parameters of the angle 2θ, FWHM, d inter-planar-spacing; D grain size, γ Dislocation density and ε strain for peaks (110) and (220)

| Material | h, k, l | 2θ (degree) | FWHM (m) | d (nm) | D (nm) | $\gamma\ 10^{-3}$ ($nm^{-2}$) | $\varepsilon\ 10^{-3}$ |
|---|---|---|---|---|---|---|---|
| $MAPbI_3$ | 110 | 14.24 | 0.30 | 6.21 | 26.51 | 1.42 | 10.55 |
| | 220 | 28.58 | 0.18 | 3.12 | 44.55 | 0.50 | 3.15 |
| | | Medium | | 4.67 | 35.53 | 0.96 | 6.85 |
| $MA_{0.7}FA_{0.3}PbI_3$ | 110 | 14.11 | 0.32 | 6.27 | 25.02 | 1.60 | 11.29 |
| | 220 | 28.36 | 0.27 | 3.14 | 30.35 | 1.08 | 4.66 |
| | | Medium | | 4.71 | 27.68 | 1.34 | 7.97 |
| $MA_{0.5}FA_{0.5}PbI_3$ | 110 | 14.13 | 0.28 | 6.26 | 28.80 | 1.21 | 9.78 |
| | 220 | 28.32 | 0.22 | 3.15 | 37.75 | 0.70 | 3.75 |
| | | Medium | | 4.70 | 33.27 | 0.95 | 6.77 |
| $MA_{0.3}FA_{0.7}PbI_3$ | 110 | 14.06 | 0.36 | 6.29 | 22.42 | 1.99 | 12.63 |
| | 220 | 28.27 | 0.28 | 3.15 | 29.26 | 1.17 | 4.85 |
| | | Medium | | 4.72 | 25.84 | 1.58 | 8.75 |
| $FAPbI_3$ | 001 | 14.05 | 0.29 | 6.30 | 27.13 | 1.36 | 10.44 |
| | 002 | 28.22 | 0.20 | 3.16 | 40.55 | 0.61 | 3.51 |
| | | Medium | | 4.73 | 33.84 | 0.98 | 6.97 |

The data in Table 1 allow us to plot the curves of the FWHM, the grain size (D), the interplanar spacing (d), the dislocation density, and the deformation, as illustrated in Figure 3 and Figure 4.

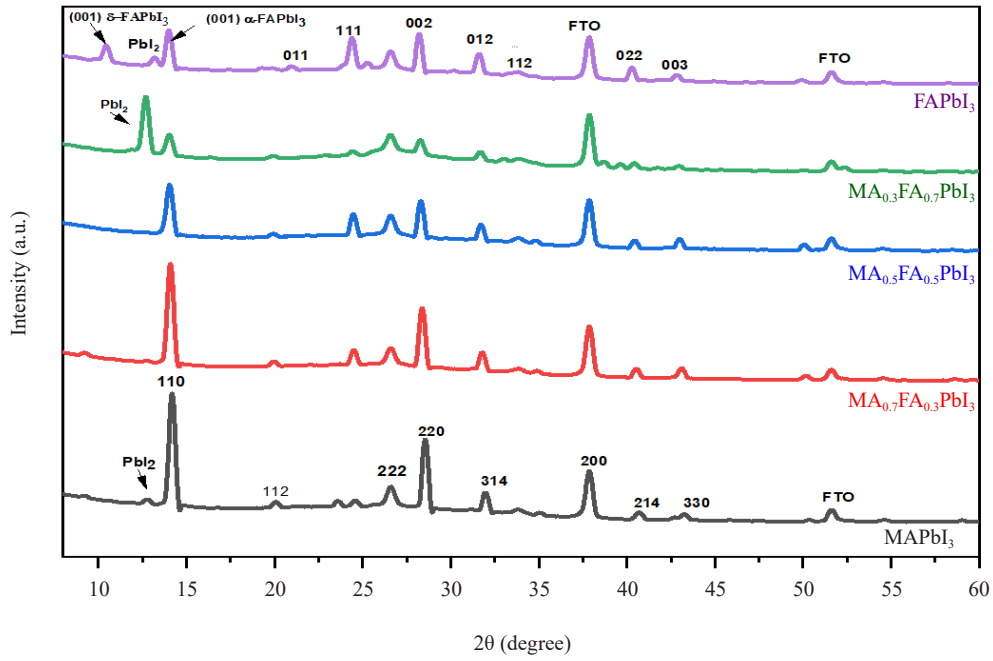


**Figure 2.** XRD patterns of $MA_{(1-x)}FA_xPbI_3$ perovskite films

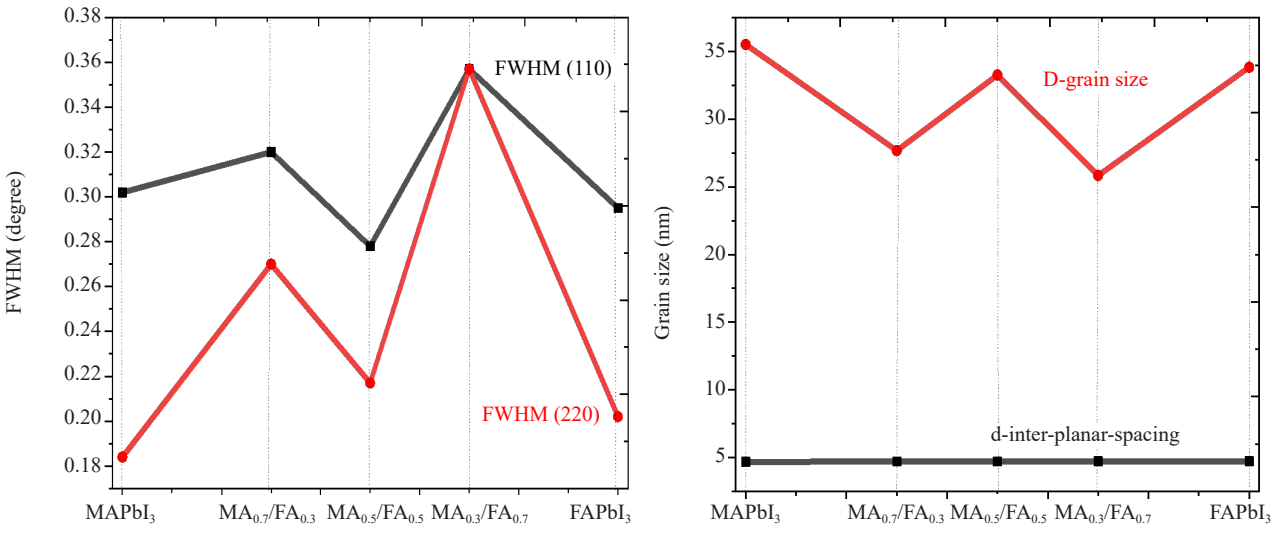


**Figure 3.** (a) FWHM of (110) and (220) peaks of $MA_{(1-x)}FA_xPbI_3$ perovskite films (b) Grain size and d-interplanar spacing peaks (110) and (220) of $MA_{(1-x)}FA_xPbI_3$ perovskite films

The FWHM represents the (110) and (220) peaks of the mixed MA/FA perovskite. The structural parameters were calculated using the Williamson-Hall (WH) plot method and are presented in Table 2 based on XRD analysis data. The 'd' value remains nearly constant for all perovskites. On the other hand, the grain size values evolve in a sawtooth pattern as the percentage of FA increases.

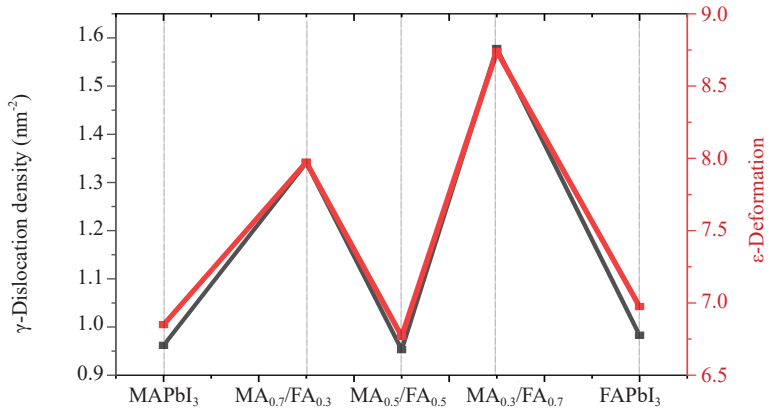


**Figure 4.** γ-Dislocation density and ε-Deformation characteristics of peaks (110) and (220) for $MA_{(1-x)}FA_xPbI_3$ perovskites

The curves of the dislocation density (γ) and the deformations (ε) share similar patterns and become more significant as the FA content increases. XRD analysis revealed that residues and degraded γ-phases of $FAPbI_3$ can be controlled by the MA/FA mixing with an appropriate amount of MA.

The SEM images displayed in Figure 5(a-e) exhibit a good morphology of perovskite films. They are observed to have excellent adhesion to the substrate, are relatively rough, and are free of pinholes. Surface roughness correlates with the amount of FA, and it is worth noting that the surface of the $MA_{0.3}FA_{0.7}PbI_3$ film is rougher with more pores than the other films. The presence of multiple pores and surface roughness allows the films to trap light [30].

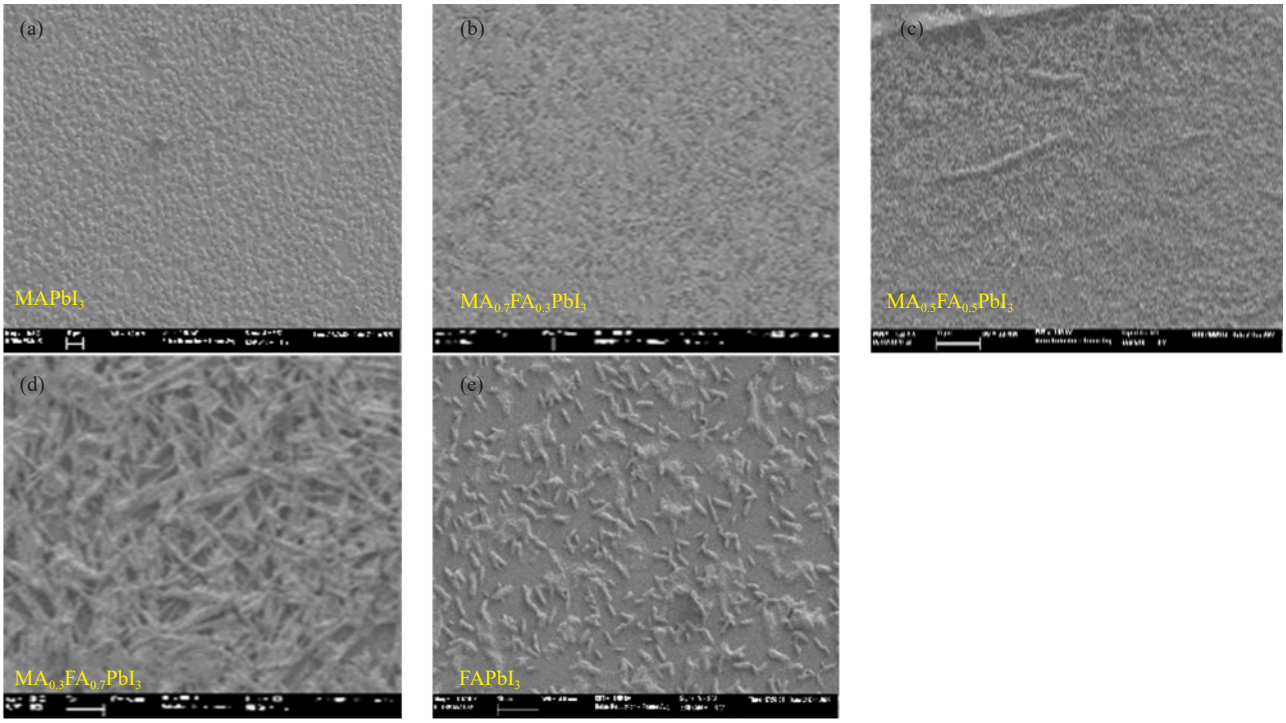


**Figure 5.** SEM images of $MA_{(1-x)}FA_xPbI_3$ perovskites films

## 3.1 *Optical properties*

Figure 6 displays the absorbance, transmission, and energy curves. The analysis of the optical properties of perovskite thin films covered the wavelength range from 400 nm to 800 nm.

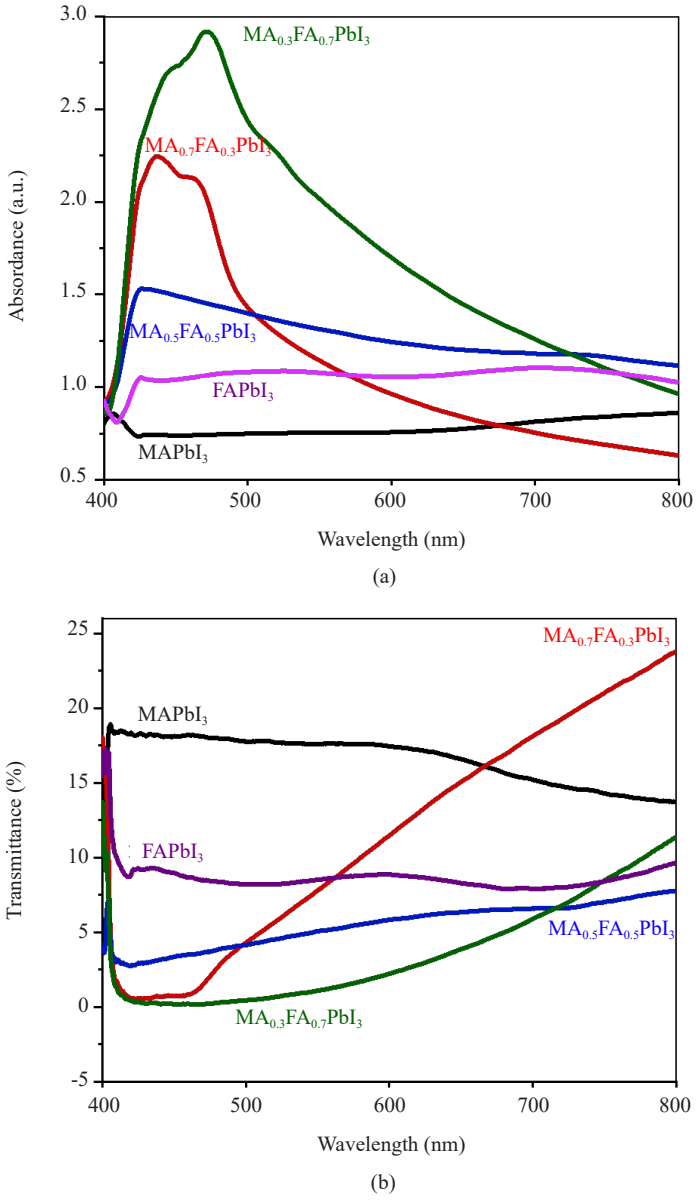


**Figure 6.** (a) absorption spectra of $MA_{(1-x)}FA_xPbI_3$ perovskites and (b) Transmission spectra of $MA_{(1-x)}FA_xPbI_3$ perovskites

Furthermore, within the 450-550 nm range, a significant increase in the absorption of the samples containing both FA and MA was observed. This increase is attributed to the abundance of electronic transitions at the vibrational or rotational energy levels, resulting in strong absorption in the visible spectrum. Mixed films exhibited higher absorbance compared to $MAPbI_3$ and $FAPbI_3$. Additionally, the incorporation of both perovskites shifted the absorption edges upward, with a maximum value of 2.9 observed for the roughest film, $MA_{0.3}FA_{0.7}PbI_3$, followed by $MA_{0.7}FA_{0.3}PbI_3$, which was the darkest sample. The enhanced absorption in these samples can be attributed to the increased crystallinity

and surface roughness of the films [31]. This is confirmed by XRD and SEM analyses. The film's rigidity optimizes the trapping of incident light.

According to Figure 7, the perovskite energy curves display optical band gaps that narrow as the FA content increases and vary in relation to the grain size. The sequence of band gap variations in descending order reflects a modification of the initial $MAPbI_3$ network parameters [32].

Transmission curves have also been plotted, with the highest value observed for $MAPbI_3$ at around 17%, and the lowest transmission occurring in the $MA_{0.3}FA_{0.7}PbI_3$ film, which reaches a minimum of 0%.

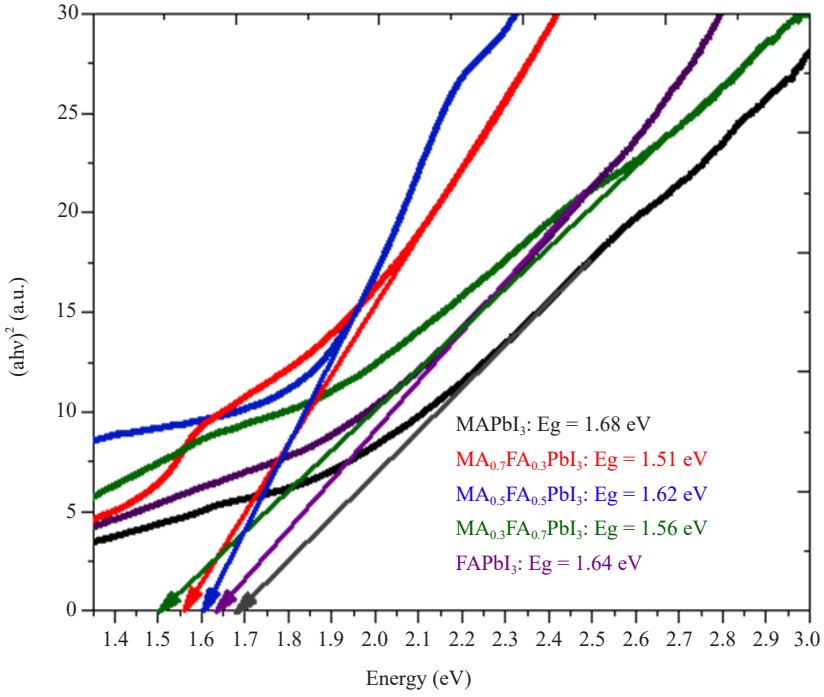


**Figure 7.** Band gap of $MA_{(1-x)}FA_xPbI_3$ perovskites

The photoluminescence spectrum allows us to determine the band gaps of the perovskite films, which can be compared with the band gaps obtained from the energy spectra.

**Table 2.** The band gap calculated from the PL and UV-Visible and shift stokes of $MA_{(1-x)}FA_xPbI_3$ Perovskites

| | $MAPbI_3$ | $MA_{0.7}FA_{0.3}PbI_3$ | $MA_{0.5}FA_{0.5}PbI_3$ | $MA_{0.3}FA_{0.7}PbI_3$ | $FAPbI_3$ |
|---|---|---|---|---|---|
| $(ahv)^2$ | 1.68 | 1.56 | 1.62 | 1.51 | 1.64 |
| PL | 1.63 | 1.58 | 1.61 | 1.59 | 1.61 |
| Shift stokes | 0.05 | 0.02 | 0.01 | 0.07 | 0.03 |

Figure 8(a, b) displays the photoluminescence (PL) emission spectra of the perovskite samples. Among them, the $FAPbI_3$ film exhibits the highest photoluminescence, followed by the $MA_{0.3}/FA_{0.7}$ mixture, both of which show significant PL emissions. Subsequently, there are lower PL emissions observed in the $MA_{0.5}/FA_{0.5}$ film, followed by

$MA_{0.7}FA_{0.3}PbI_3$ has the lowest PL emission and corresponds to the darkest sample.

The weak emission from $MAPbI_3$ can be attributed to the reduced density of surface trap states, resulting in a decrease in non-radiative pathways [33]. Consequently, recombination occurs during the radiative stage [34]. The photoluminescence spectra of the MA/FA mixtures are consistent with the XRD and SEM results.

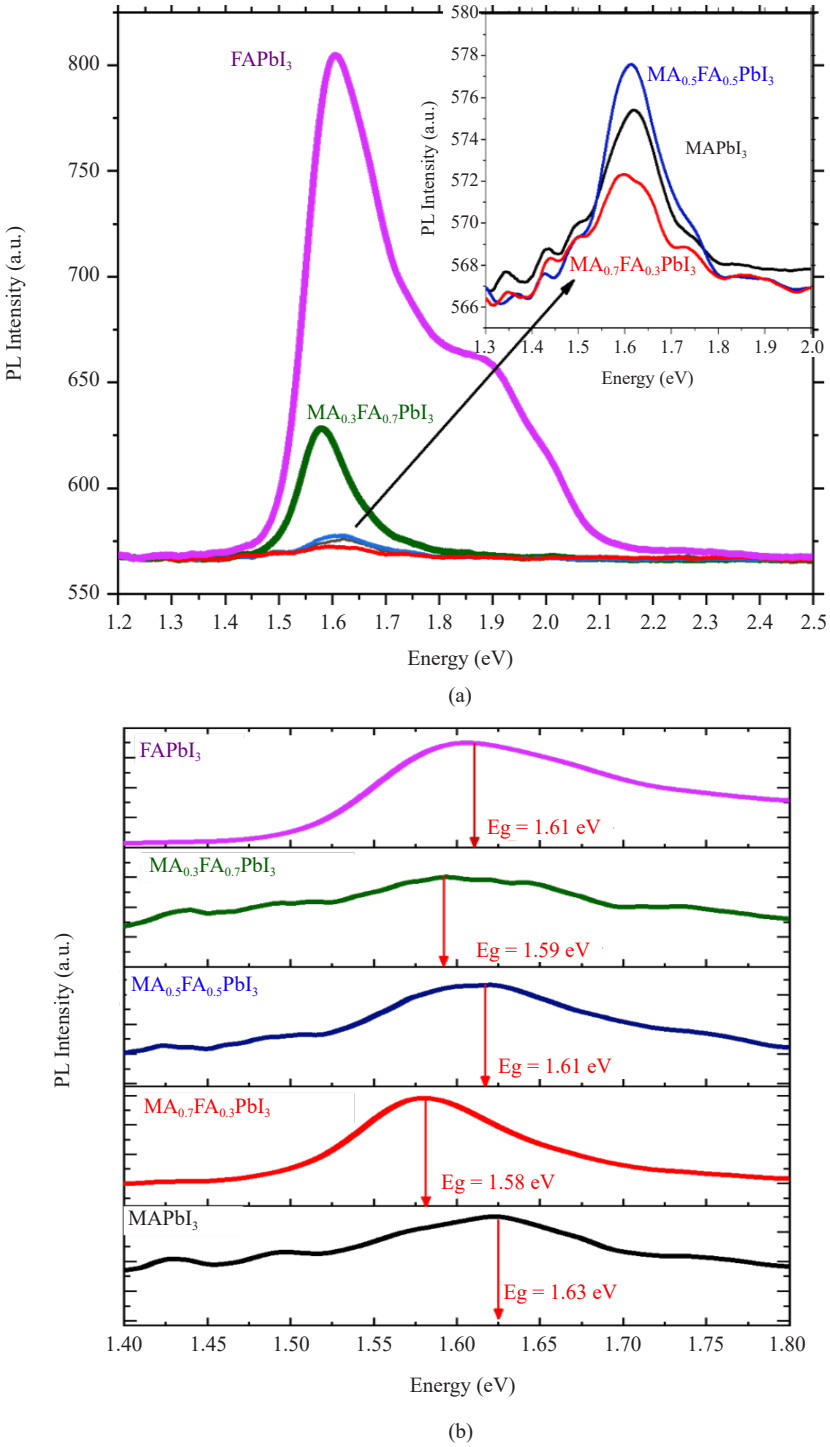


**Figure 8.** Photoluminescence of $MA_{(1-x)}FA_xPbI_3$ perovskites (a) and band gap values calculated by PL peak emission of $MA_{(1-x)}FA_xPbI_3$ perovskites

Table 2 summarizes the optical band gap (Eg) values of $MA_{(1-x)}FA_xPbI_3$, extracted from UV and PL measurements. The absorption edge decreases slightly from 1.68 to 1.51 eV as the FA content is increased. The band gaps of the PL in the perovskite films range between 1.63 and 1.58 eV.

The electrical resistivity of the samples was measured with an uncertainty error of 0.02 using the four-point probe method based on the Hall effect [35-37]. To determine the resistivity of the perovskites, deposits were spin-coated onto simple glass substrates without FTO, resulting in thicknesses of approximately 500 nm. The electrical resistivity (ρ) is calculated using the equation: $\rho = Rs \times t$, where 't' represents the thickness and 'Rs' is the resistivity of the thin film. 'Rs' is determined as the surface resistance of the film, given by $Rs = 4.5324 \times (V/I)$, with 4.532 as the correction factor. We conclude that mixing MA with FA did not have any influence on the conductivity or resistivity.

**Table 3**. Resistivities and conductivities values of $MA_{(1-x)}FA_xPbI_3$ perovskites

| Sample | U/I ($10^6$ V/A) | Rs (Ω/sq) | $\rho$ resistivity (Ω·cm) | Conductivity ($10^{-5}$ 1/Ω·cm) |
|---|---|---|---|---|
| $MAPbI_3$ | 1.00 | 4.55 | 227.89 | 438.81 |
| $MA_{0.7}FA_{0.3}PbI_3$ | 0.99 | 4.52 | 226.08 | 442.33 |
| $MA_{0.5}FA_{0.5}PbI_3$ | 0.99 | 4.50 | 225.12 | 444.20 |
| $MA_{0.3}FA_{0.7}PbI_3$ | 0.99 | 4.49 | 224.75 | 445.01 |
| $FAPbI_3$ | 0.99 | 4.48 | 224.35 | 445.72 |

The measurement of perovskite resistance is conducted with an intensity on the order of nanovolts. For high-intensity values, the passage of current through the films leads to a modification of their structure. Additionally, with prolonged exposure to the electrodes, the films heat up, which can affect the measurements. We obtained resistivity values for the thin films on the order of 200 Ω·cm, and they vary slightly. The smallest value is observed for $FAPbI_3$. The high resistivity values are attributed to the organic nature of the studied perovskites. The resistivity and the mobility of charge carriers in the perovskite layers are determined, as shown in Table 3.

The measurement of the films' resistivity yields values that are very close to each other, as do the conductivity values. To clearly observe the shift in resistivity, their values have been scaled down by a factor of 224. Similarly, for conductivity, their values have been scaled down by a factor of 438. The obtained curves show that the resistivity values decrease slightly as the FA content increases.

## 4. Degradation study

SEM images are displayed in Figure 9. The degradation is evident with several pinholes and significant changes in surface morphology across the films. The image of the most degraded sample corresponds to pure and aged $MAPbI_3$. After three weeks in a humid environment, the film morphology images reveal a reduction in degradation as the FA content increases in the mixture. This observation aligns with the results obtained from XRD and absorption spectra, affirming the stability of the mixed films in relation to the $FAPbI_3$ content. Additionally, the mixing process stabilizes the black phase of $FAPbI_3$, resulting in improved XRD spectra and the suppression of the phase-δ transition.

The $MA_{0.3}/FA_{0.7}$ mixture appears to play a significant role in slowing down the degradation of $FAPbI_3$ thin films, as shown in Figure 10. Furthermore, the absorption and optical properties of the mixed films exhibit good agreement, contributing to the enhancement of performance and stability in $MAPbI_3$ films.

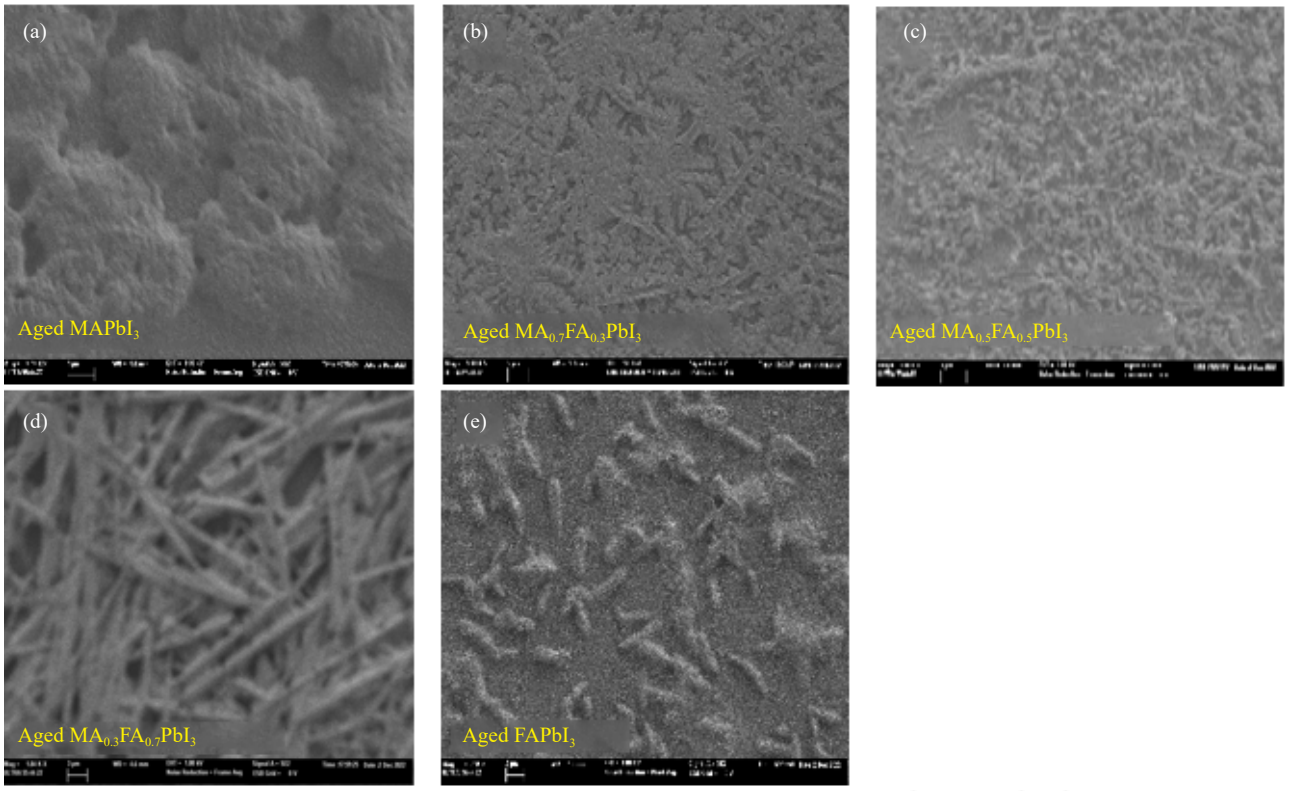


**Figure 9.** SEM images of three-week-aged $MA_{(1-x)}FA_xPbI_3$ perovskite films

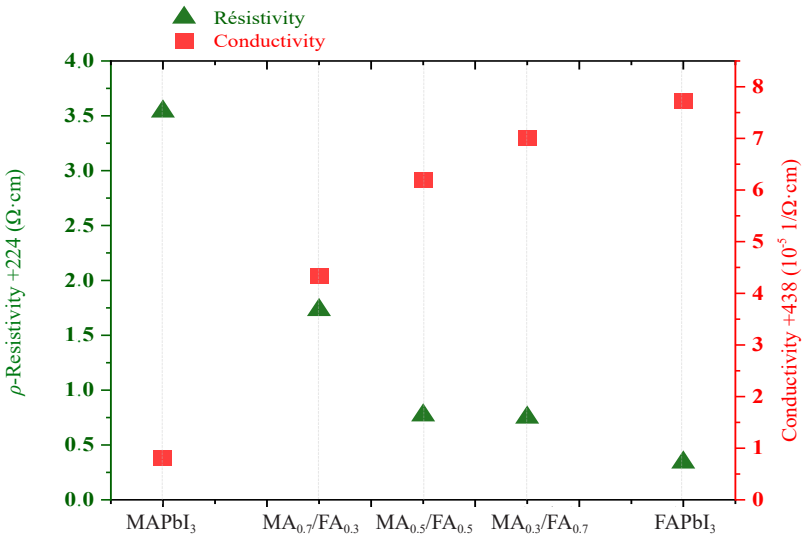


**Figure 10.** Resistivity and conductivity of $MA_{(1-x)}FA_xPbI_3$ perovskites

The degradation mechanism of the XRD pattern was examined for all aged samples, as shown in Figure 11(a-e). Over the course of three weeks in a humid environment, the films exhibited degradation. The presence of lead in the aged samples is clearly illustrated by a significant increase in its characteristic peak located at 12.6 degrees, accompanied by a decrease in the characteristic peaks of perovskites (110) and (220) located at 14.24 and 28.58 degrees,

respectively.

The impact of aging on the characteristic peaks diminishes as the proportion of FA increases in the films. The spectra exhibit a noticeable reduction in degradation for both the $MA_{0.3}/FA_{0.7}$ mixture and $FAPbI_3$. The incorporation of MA and FA into the perovskite structure proves to be an effective method for controlling degradation and preventing the undesired δ-phase formation in $FAPbI_3$ by slowing down the dissociation of $MAPbI_3$ and $FAPbI_3$ into their $PbI_2$ precursors.

The XRD spectrum of the $MA_{0.3}/FA_{0.7}$ mixture shows a slight decrease in the characteristic peak intensities compared to the other films. These XRD results align with measurements of the absorption of the aged films, which demonstrate a significant reduction in absorption intensities. The mixtures exhibit significant absorption intensities in increasing order corresponding to the FA concentration in the mixtures.

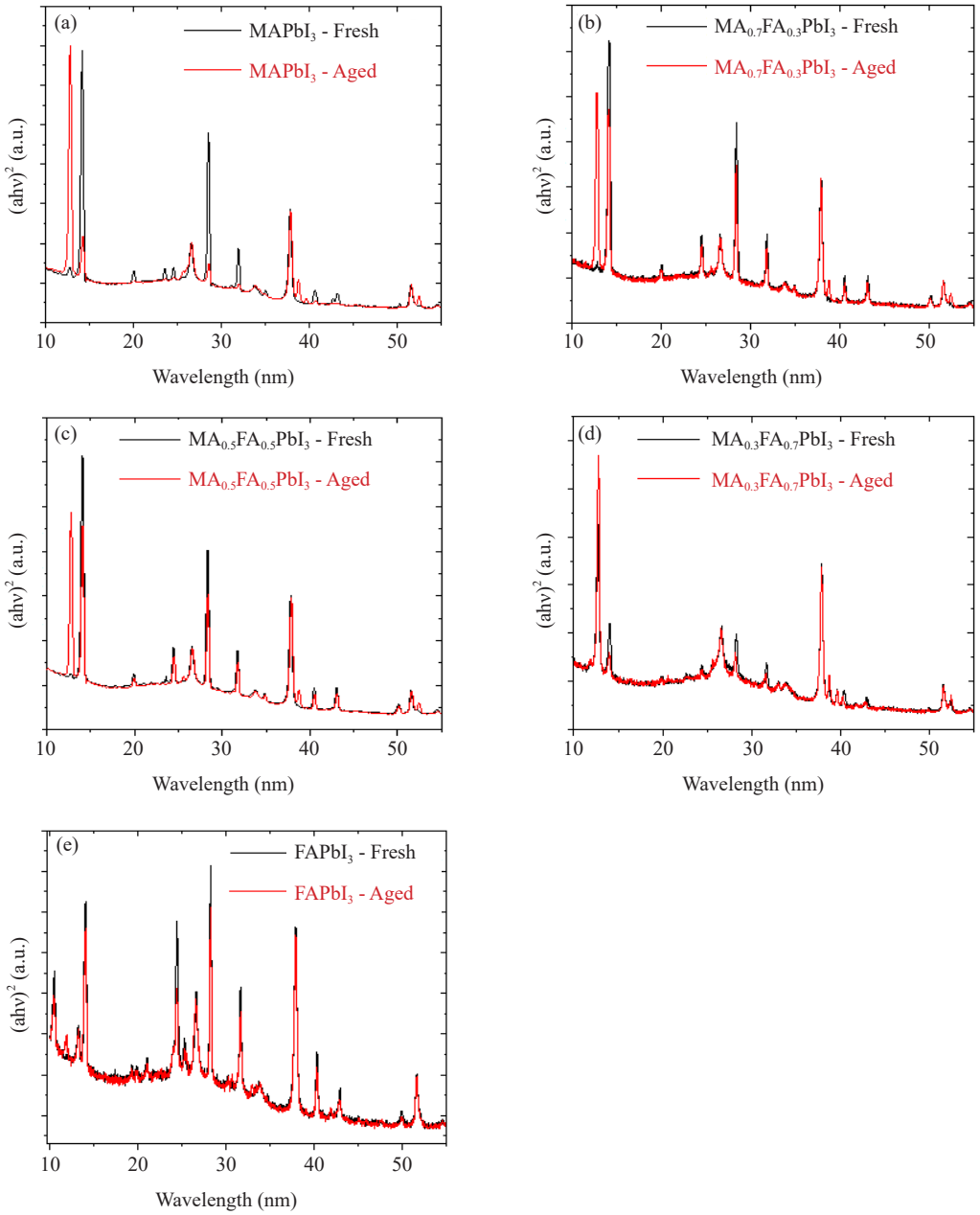


**Figure 11.** XRD patterns of both fresh and aged $MA_{(1-x)}FA_xPbI_3$ perovskites

Figure 12 displays the absorption spectra of aged perovskite films exposed to open air in a humid and dark environment for three weeks. A reduction in absorption is observed in all samples. However, the $MA_{0.3}/FA_{0.7}$ mixture exhibits the highest absorption, followed by the $MA_{0.5}/FA_{0.5}$ mixture. $FAPbI_3$ is in the third position, and the absorption curves of $MAPbI_3$ and the $MA_{0.7}/FA_{0.3}$ mixture overlap with consistent values. Notably, strong absorptions are observed near 450 nm.

In mixed films, a higher FA content corresponds to a slower degradation rate. The decrease in absorption is visually confirmed by comparing photographs of fresh films to films aged in the open air in a dark and humid environment for three weeks. The colors transition from black-grey to green for the $MA_{0.7}/FA_{0.3}$ mixture, from black to green-grey for the $MA_{0.3}/FA_{0.7}$ mixture, and from dark brown to light brown for $FAPbI_3$, indicating significant degradation compared to fresh films. Additionally, there is a change in the coloration of the $MA_{0.5}/FA_{0.5}$ mixture, shifting from gray to brown and back to gray, and of the $MA_{0.3}/FA_{0.7}$ mixture, changing from a lighter brown to a lighter shade. These films exhibit less degradation compared to $MAPbI_3$ and the $MA_{0.7}/FA_{0.3}$ mixture, which are completely degraded under the same conditions. These absorption results from degraded samples align with the XRD results of the aged films. The FA content in the mixtures influences the degradation process [38-44].

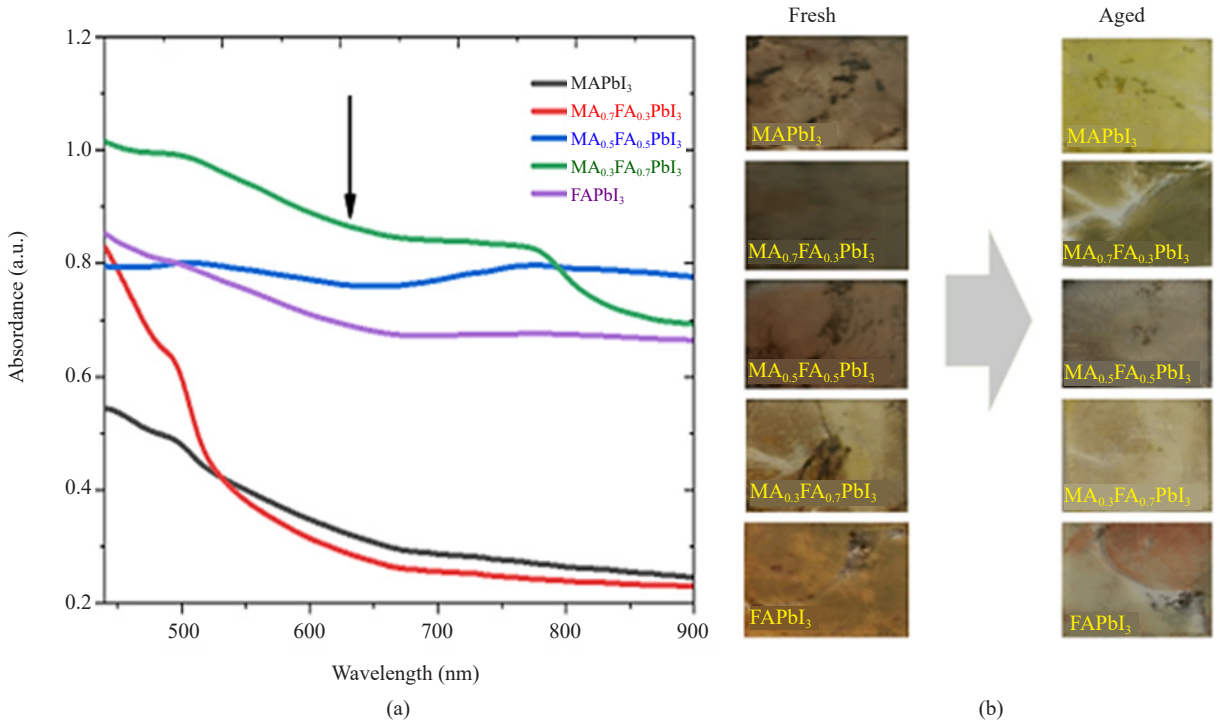


**Figure 12.** Photographs of fresh and aged films, and absorption spectra after three weeks of $MA_{(1-x)}FA_xPbI_3$ perovskites

## 5. Conclusion

In this work, we conducted a study to optimize the MA/FA ratio within the structure of $MA_{(1-x)}FA_xPbI_3$ perovskites with the aim of stabilizing $MAPbI_3$. $MAPbI_3$ exhibits favorable optical properties but lower stability compared to $FAPbI_3$. The results indicate that incorporating 70% of $FAPbI_3$ considerably improves the crystallinity and morphology of the perovskite film. The introduction of FA contributes to homogenizing and roughening the film's surface, enabling it to efficiently capture incident light.

XRD results demonstrate that the presence of FA enhances characteristic peaks, reduces residual $PbI_2$, and suppresses the formation of the $FAPbI_3$ phase. SEM images show that all thin films have relatively rough surfaces. Additionally, band gaps decrease slightly from 1.68 to 1.51 eV as the FA content increases, while absorption curves

decrease as the FA content decreases. The band gaps obtained through photoluminescence analysis closely correspond to those obtained through absorption.

It is noteworthy that degradation leads to reduced absorption in the films and a lower density of trap states in the samples. Degradation causes the perovskites to decompose into their precursors, such as $PbI_2$. However, the presence of FA slows down the degradation process in a humid environment by preventing the formation of $PbI_2$ compounds, particularly those of the γ-$FAPbI_3$ phase.

These results contribute to a fundamental understanding of the mechanisms underlying perovskite degradation and provide strategies for designing stable and high-performance perovskite-based devices. Our interest in FA stems from its demonstrated stability.

The optical properties are improved, and the mixed thin film exhibits greater stability compared to pure $MAPbI_3$ and $FAPbI_3$ thin films. The characteristics of the films suggest that these mixtures are particularly well-suited for use in photovoltaic applications.

## Acknowledgement

Diomande Idrissa acknowledged erasmus107 for the grant, The author Amal Bouich acknowledges MCIN for funding support through Margarita Salas Fellowship (MCIN/AEI/10.13039/501100011033). This research has been funded by Grant PID2019-107137RB-C22 funded by MCIN/AEI/10.13039/501100011033 and by ERDF A Way of Making Europe. This research has been funded by Grant PID2019-107137RB-C22 funded by MCIN/AEI/10.13039/501100011033 and by ERDF A way of making Europe. This research has been funded by Aero.Next Portugal - ILAN VR funded by C645727867-00000066 by UniversaPulsar Spinoff of University of Évora.

## Conflict of interest

The authors declare that they have no conflict of interest.

## References

[1] Ma XX, Li ZS. Influence of Sn/Ge cation exchange on vacancy-ordered double perovskite $Cs_2Sn_{(1-x)}Ge_xI_6$: A first-principles theoretical study. *Physica Status Solidi (B)*. 2019; 256(3): 1800427.

[2] Gao F, Zhao Y, Zhang X, You J. Recent progresses on defect passivation toward efficient perovskite solar cells. *Advanced Energy Materials*. 2020; 10(13): 1902650.

[3] Min H, Lee DY, Kim J, Kim G, Lee KS, Kim J, et al. Perovskite solar cells with atomically coherent interlayers on $SnO_2$ electrodes. *Nature*. 2021; 598(7881): 444-450.

[4] Furasova A, Voroshilov P, Sapori D, Ladutenko K, Barettin D, Zakhidov A, et al. Nanophotonics for perovskite solar cells. *Advanced Photonics Research*. 2022; 3(9): 2100326.

[5] Liu H, Yu MH, Lee CC, Yu X, Li Y, Zhu Z, et al. Technical challenges and perspectives for the commercialization of solution-processable solar cells. *Advanced Materials Technologies*. 2021; 6(6): 2000960.

[6] Lu X, Morelli DT, Xia Y, Zhou F, Ozolins V, Chi H, et al. High performance thermoelectricity in earth-abundant compounds based on natural mineral tetrahedrites. *Advanced Energy Materials*. 2013; 3(3): 342-348.

[7] Al-Asbahi BA, Qaid SM, Hezam M, Bedja I, Ghaithan HM, Aldwayyan AS. Effect of deposition method on the structural and optical properties of $CH_3NH_3PbI_3$ perovskite thin films. *Optical Materials*. 2020; 103: 109836.

[8] Baldo M, Deutsch M, Burrows P, Gossenberger H, Gerstenberg M, Ban V, et al. Organic vapor phase deposition. *Advanced Materials*. 1998; 10(18): 1505-1514.

[9] Sukharevska N, Bederak D, Goossens VM, Momand J, Duim H, Dirin DN, et al. Scalable PbS quantum dot solar cell production by blade coating from stable inks. *ACS Applied Materials & Interfaces*. 2021; 13(4): 5195-5207.

[10] Vashishtha P, Bishnoi S, Li CH, Jagadeeswararao M, Hooper TJ, Lohia N, et al. Recent advancements in near-infrared perovskite light-emitting diodes. *ACS Applied Electronic Materials*. 2020; 2(11): 3470-3490.

[11] Omidvar A, Jaleh B, Nasrollahzadeh M. Preparation of the GO/Pd nanocomposite and its application for the

degradation of organic dyes in water. *Journal of Colloid and Interface Science*. 2017; 496: 44-50.
[12] Rehman W, McMeekin DP, Patel JB, Milot RL, Johnston MB, Snaith HJ, et al. Photovoltaic mixed-cation lead mixed-halide perovskites: links between crystallinity, photo-stability and electronic properties. *Energy & Environmental Science*. 2017; 10(1): 361-369.
[13] Bouich A, Torres JC, Khattak YH, Baig F, Marí-Guaita J, Soucase BM, et al. Bright future by controlling α/δ phase junction of formamidinium lead iodide doped by imidazolium for solar cells: Insight from experimental, DFT calculations and SCAPS simulation. *Surfaces and Interfaces*. 2023; 40: 103159.
[14] Rao MK, Sangeetha DN, Selvakumar M, Sudhakar YN, Mahesha MG. Review on persistent challenges of perovskite solar cells' stability. *Solar Energy*. 2021; 218: 469-491.
[15] Sutherland LJ, Weerasinghe HC, Simon GP. A review on emerging barrier materials and encapsulation strategies for flexible perovskite and organic photovoltaics. *Advanced Energy Materials*. 2021; 11(34): 2101383.
[16] Ünlü F, Jung E, Öz S, Choi H, Fischer T, Mathur S. Chemical processing of mixed-cation hybrid perovskites: Stabilizing effects of configurational entropy. *Perovskite Solar Cells: Materials, Processes, and Device*s. 2021; 1-31.
[17] Zhang H, Chen Z, Li Y, Yao J, Liu D, Zeng W, et al. A high-performance self-powered photodetector based on a concentric annular α-$FAPbI_3$/$MAPbI_3$ single crystal lateral heterojunction with broadband detectivity. *Journal of Materials Chemistry C*. 2022; 10(33): 11903-11913.
[18] Raeisianasl M, Panahi SF, Jamaati M, Tafreshi SS. A review on theoretical studies of structural and optoelectronic properties of FA-based perovskite materials with a focus on $FAPbI_3$. *International Journal of Energy Research*. 2022; 46(10): 13117-13151.
[19] Liu Y, Zhang Y, Zhu X, Feng J, Spanopoulos I, Ke W, et al. Triple-cation and mixed-halide perovskite single crystal for high-performance X-ray imaging. *Advanced Materials*. 2021; 33(8): 2006010.
[20] Suzuki A, Oku T. Effects of mixed-valence states of Eu-doped $FAPbI_3$ perovskite crystals studied by first-principles calculation. *Materials Advances*. 2021; 2(8): 2609-2616.
[21] Zhang C, Gao L, Hayase S, Ma T. Current advancements in material research and techniques focusing on lead-free perovskite solar cells. *Chemistry Letters*. 2017; 46(9): 1276-1284.
[22] Limpamanoch P, Rujisamphan N, Kumnorkaew P, Amornkitbamrung V, Tang IM, Zhang Q, et al. Understanding effects of cesium in $CH(NH_2)_2PbI_3$ for stabilizing $CH(NH_2)_2PbI_3$/$CsPbI_3$ interface under UV illumination. *The Journal of Physical Chemistry C*. 2019; 123(19): 12117-12125.
[23] Salado M, Calio L, Berger R, Kazim S, Ahmad S. Influence of the mixed organic cation ratio in lead iodide-based perovskite on the performance of solar cells. *Physical Chemistry Chemical Physics*. 2016; 18(39): 27148-27157.
[24] Cui P, Wei D, Ji J, Huang H, Jia E, Dou S, et al. Planar p-n homojunction perovskite solar cells with efficiency exceeding 21.3%. *Nature Energy*. 2019; 4(2): 150-159.
[25] Basumatary P, Agarwal P. Photocurrent transient measurements in $MAPbI_3$ thin films. *Journal of Materials Science: Materials in Electronics*. 2020; 31: 10047-10054.
[26] Kumar GR, Savariraj AD, Karthick SN, Selvam S, Balamuralitharan B, Kim HJ, et al. Phase transition kinetics and surface binding states of methylammonium lead iodide perovskite. *Physical Chemistry Chemical Physics*. 2016; 18(10): 7284-7292.
[27] Hu X, Zhu C, Zhang W, Wang H, Wang J, Ren F, et al. Strain release of formamidinium-cesium perovskite with imprint-assisted organic ammonium halide compensation for efficient and stable solar cells. *Nano Energy*. 2022; 101: 107594.
[28] Tailor NK, Kar S, Mishra P, These A, Kupfer C, Hu H, et al. Advances in lead-free perovskite single crystals: Fundamentals and applications. *ACS Materials Letters*. 2021; 3(7): 1025-1080.
[29] Hu M, Liu L, Mei A, Yang Y, Liu T, Han H. Efficient hole-conductor-free, fully printable mesoscopic perovskite solar cells with a broad light harvester $NH_2CH$ [double bond, length as m-dash] $NH_2$ $PbI_3$. *Journal of Materials Chemistry A*. 2014; 2(40): 17115-17121.
[30] Durmanov NN, Guliev RR, Eremenko AV, Boginskaya IA, Ryzhikov IA, Trifonova EA, et al. Non-labeled selective virus detection with novel SERS-active porous silver nanofilms fabricated by Electron Beam Physical Vapor Deposition. *Sensors and Actuators B: Chemical*. 2018; 257: 37-47.
[31] Turner ST, Pingel P, Steyrleuthner R, Crossland EJ, Ludwigs S, Neher D. Quantitative analysis of bulk heterojunction films using linear absorption spectroscopy and solar cell performance. *Advanced Functional Materials*. 2011; 21(24): 4640-4652.
[32] Kulkarni SA, Baikie T, Boix PP, Yantara N, Mathews N, Mhaisalkar S. Bandgap tuning of lead halide perovskites using a sequential deposition process. *Journal of Materials Chemistry A*. 2014; 2(24): 9221-9225.
[33] Fassl P, Zakharko Y, Falk LM, Goetz KP, Paulus F, Taylor AD, et al. Effect of density of surface defects on

photoluminescence properties in $MAPbI_3$ perovskite films. *Journal of Materials Chemistry C*. 2019; 7(18): 5285-5292.
[34] Alekperova EE, Valov YA, Goryunova NA, Ryvkin SM, Shpenkov GP. Recombination radiation spectra in $ZnSiP_2$ crystals. *Physica Status Solidi (B)*. 1969; 32(1): 49-54.
[35] Petersen DH, Hansen O, Lin R, Nielsen PF. Micro-four-point probe Hall effect measurement method. *Journal of Applied Physics*. 2008; 104(1).
[36] Bouich A, Marí-Guaita J, Soucase BM, Palacios P. Manufacture of high-efficiency and stable lead-free solar cells through antisolvent quenching engineering. *Nanomaterials*. 2022; 12(17): 2901.
[37] Bouich A, Marí-Guaita J, Sahraoui B, Palacios P, Marí B. Tetrabutylammonium (TBA)-doped methylammonium lead iodide: high quality and stable perovskite thin films. *Frontiers in Energy Research*. 2022; 10: 840817.
[38] Shafi MA, Khan L, Ullah S, Bouich A, Ullah H, Mari B. Synthesis of CZTS kesterite by pH adjustment in order to improve the performance of CZTS thin film for photovoltaic applications. *Micro and Nanostructures*. 2022; 164: 107185.
[39] Bouich A, Torres JC, Chfii H, Marí-Guaita J, Khattak YH, Baig F, et al. Delafossite as hole transport layer a new pathway for efficient perovskite-based solar cells: Insight from experimental, DFT and numerical analysis. *Solar Energy*. 2023; 250: 18-32.
[40] Doumbia Y, Bouich A, Soucasse BM, Soro D. Boosting the stability and growth of methylammonium lead bromide perovskites film doped with FA for solar cells. *Optical Materials*. 2023; 137: 113563.
[41] Touré A, Bouich A, Soucasse BM, Soro D. Investigation of the optoelectronics properties and stability of formamidinium lead mixed halides perovskite. *Optical Materials*. 2023; 135: 113334.
[42] Bouri N, Talbi A, Khaaissa Y, Derbali S, Bouich A, Nouneh K. Insight into $MAPb_{1-x}Eu_xI_3$ based perovskite solar cell performance using SCAPS Simulator. *Optik*. 2022; 271: 170235.
[43] Koné KE, Bouich A, Soucase BM, Soro D. Manufacture of different oxides with high uniformity for copper zinc tin sulfide (CZTS) based solar cells. *Journal of Molecular Graphics and Modelling*. 2023; 121: 108448.
[44] Koné KE, Bouich A, Soro D, Soucase BM. Insight of ZnO/CuO and $ZnO/Cu_2O$ solar cells efficiency with SCAPS simulator. *Optical and Quantum Electronics*. 2023; 55(7): 616.